

Modelling flux variability from internal shocks in relativistic jets

Gaëtan Fichet de Clairfontaine

LUTH, Observatoire de Paris, CNRS, PSL, Université de Paris; 5 Place Jules Janssen, 92190 Meudon, France

E-mail: gaetan.fichetdeclairfontaine@obspm.fr

Zakaria Meliani

LUTH, Observatoire de Paris, CNRS, PSL, Université de Paris; 5 Place Jules Janssen, 92190 Meudon, France

E-mail: zakaria.meliani@obspm.fr

Andreas Zech*

LUTH, Observatoire de Paris, CNRS, PSL, Université de Paris; 5 Place Jules Janssen, 92190 Meudon, France

E-mail: andreas.zech@obspm.fr

Particle acceleration at stationary and moving internal shocks is one of the principal mechanisms to explain the variable emission, seen from the radio to the γ -ray band, from relativistic jets in radio-loud active galactic nuclei. To reproduce the synchrotron light curves associated with these shocks, we perform SRMHD simulations of magnetised relativistic transverse-structured jets using the AMRVAC code. Perturbations are injected at the base of a steady jet that carries stationary shocks to study the interaction between the moving and the stationary shocks. Synchrotron emission and radiative transfer are simulated in post-treatment. In a first application, the radio core of the radio-galaxy M 87 is modelled to study the flux evolution from such perturbations in the radio band and compare them against archival data.

High Energy Phenomena in Relativistic Outflows VII - HEPRO VII

9-12 July 2019

Facultat de Física, Universitat de Barcelona, Spain

*Speaker.

1. Introduction

Relativistic jets and outflows are astrophysical phenomena that occur over a large range of spatial scales, from sub-pc and pc jets in gamma-ray bursts and micro-quasars to kpc jets and Mpc-scale radio lobes in radio-loud active galactic nuclei (AGN). They are sites of efficient particle acceleration and sources of non-thermal emission from the radio band to very high energies. Different particle acceleration mechanisms, such as internal shocks, reconnection, and acceleration on shear layers or turbulence, have been suggested to explain the highly relativistic particle populations in jets.

Radio-loud AGN, i.e. radio-galaxies and blazars, are characterised by rapid flux variability (flares), observed over the whole electromagnetic spectrum and at various time scales. We are developing an SRMHD model for AGN jets that includes the treatment of radiative processes, in order to explain such flares through the interaction of relativistic ejecta from the base of the jet with standing shocks. The latter arise naturally through recollimation in a stratified jet. Such a stratification, perpendicular to the jet axis, is indicated by observations of AGN jets at different wavelengths [Avachat et al. (2016), Giroletti et al. (2014), Siemiginowska et al. (2007)].

There is also some evidence for the existence of structured large-scale magnetic fields [Asada et al. (2002), Motter et al. (2017)] which are commonly evoked to explain the stability of collimated jets over large distances. We investigate the impact different magnetic field structures have on the shape of the flare light curve. In a first application of the model, we reproduce a radio flare detected in the VLBI core of the nearby radio-galaxy M 87 in 2008.

2. Setup of the MHD code and post-processing

The MPI-AMRVAC code [Keppens et al. (2012)] is used to resolve the relativistic MHD equations with an adaptive mesh. In order to solve the *Riemann Problem*, the code uses an *HLLC* (*Harten, Lax, van Leer Contact*, [Toro et al. (1994)]) method. For faster execution, the code has been adapted to be used on super-calculators (with the *Occigen*¹ or the *Meso-PSL* machine² in our case). The simulated jet is stratified as shown in Fig. 1, with an over-pressured inner jet (IJ), with a factor of ~ 1.5 higher pressure relative to the ambient matter (AM) and the outer jet (OJ), allowing the formation of standing shocks [Hervet et al.(2017)].

Density increases from the inner jet ($\sim 10^{-3}$ relative to AM) to the OJ ($\sim 10^{-2}$ relative to the ambient medium). In terms of the injected energy, we assume a ratio of $\sim 10^3$ between the OJ and the IJ, with a total energy at $\sim 10^{46}$ erg/s. The difference in pressure between the IJ and AM leads to the appearance of recollimation shocks along the jet. The magnetic configuration is given by the angle between the poloidal and the toroidal component and by the magnetisation σ . All our general jet simulations have the same initial parameters to allow for a direct comparison. We study the effect of transverse stratification and magnetic field configuration of the jet on the variability, through injection of spherical over-densities at the base of the IJ, which interact with the standing shocks. The spherical perturbations (or “ejecta”) are added only once the jet has reached its stationary state.

¹See <http://www.cines.fr>

²See <http://www.mesopsl.fr>

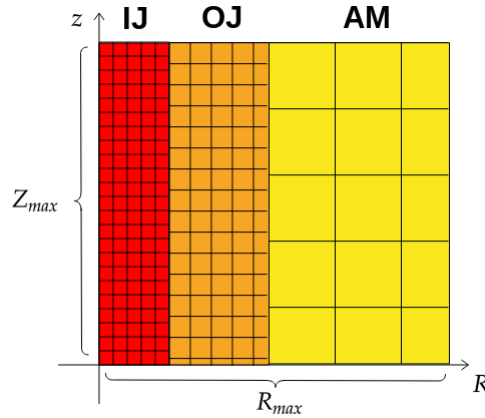


Figure 1: Layout of the simulated cells.

In a post-processing step, we inject in the compression zones (stationary and mobile) a population of relativistic electrons following [Gomez et al. (1995)]. Simulated 2D maps are extracted from MPI-AMRVAC in the form of vtk files.

Using approximations for the synchrotron emissivity and absorption coefficient to reduce CPU time [Katarzynski et al. (2001)], the synchrotron flux in the observer frame is calculated, taking into account relativistic effects and radiative transfer between all the cells along each line of sight for a given jet viewing angle. We determine maps of the observed synchrotron flux at fixed time steps ("snapshots") and produce light curves of the evolution of the total observed synchrotron flux due to the passage of ejecta through standing shocks. At present, corrections for light-travel time inside the jet and for radiative cooling are neglected.

3. Solutions for different magnetic field geometries

3.1 The purely hydrodynamic case

As a reference, a first simulation was run assuming the absence of any large-scale magnetic field. A turbulent magnetic field was added in the post-processing for this scenario. A fraction of the thermal energy density of the particles ($\sim 1\%$) is assigned to the turbulent magnetic energy density.

On the density map (Fig. 2, right), the IJ, OJ and AM are clearly visible due to the increase of density. An ejecta can be seen in the inner jet (at distances ~ 3 pc from the base) and also in the 1D profile traced along the z axis (Fig. 3). The pressure map (Fig. 2, left) shows a succession of stationary compression zones and the mobile compression zone associated to the ejecta. As it travels along the jet, the ejecta is subject to a transverse deformation due to its interactions with the shock structure inside the inner jet and with the matter inside the different components.

Based on the hydrodynamical case, it was found that the geometrical structure of the jet plays an important role [Hervet et al.(2017)]. The presence of an external jet component limits the transverse deformation of the ejecta : the transverse structure of the jets changes the position and the intensity of the internal shocks. This structure enables the collimation of ejecta over long distances.

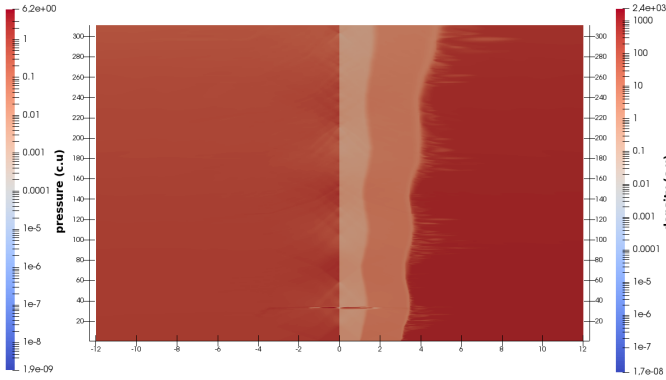


Figure 2: Snapshot: structured hydrodynamic jet with one ejecta. Pressure map on the left, density map on the right. Units on x- and y-axis in 0.1 pc.

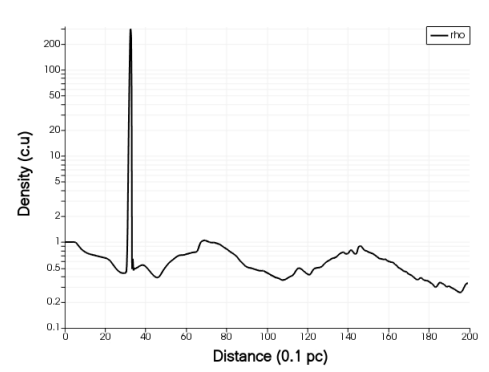


Figure 3: Profile of the density (log) in the inner jet along the propagation axis. Units on x-axis in 0.1 pc.

3.2 The poloidal case

The density map for a poloidal magnetic field (field lines in the direction of the jet axis, $B \sim 0.1$ G; Fig. 4, right) shows the same transverse structure as in the hydrodynamic case. An ejecta in the IJ is visible on the 1D profile (at a distances of ~ 3 pc). On the pressure map (Fig. 4, left), a more complex structure of stationary and moving compression zones appears due to the poloidal configuration. The presence of oblique shock waves propagating through the jet induces compressive forces destabilizing the jet. It should be noted that a certain degree of fine tuning of the jet parameters is necessary in this case to obtain a stable stationary solution.

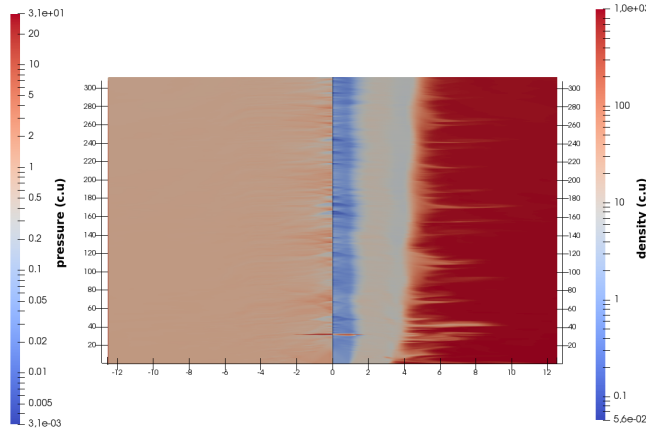


Figure 4: Snapshot: structured poloidal jet with an ejecta. Pressure map on the left, density map on the right. Units on x- and y-axis in 0.1 pc.

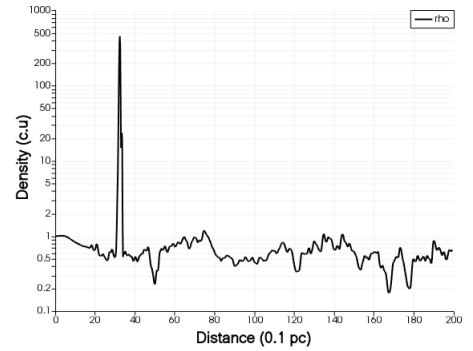


Figure 5: Profile of the density (log) in the inner jet along the propagation axis. Units on x-axis in 0.1 pc.

This magnetic configuration leads to a magnetic pressure along the z -axis (propagation axis) that compresses the ejecta. The magnetic field permits to collimate the ejecta within the inner jet, leading to a less important transverse energy loss than in the hydrodynamic case. Finally, we notice that this magnetic configuration induces internal shocks of lower intensity. In this case, the ejecta are less accelerated, which may explain why the transverse dissipation of energy is lower.

3.3 The toroidal case

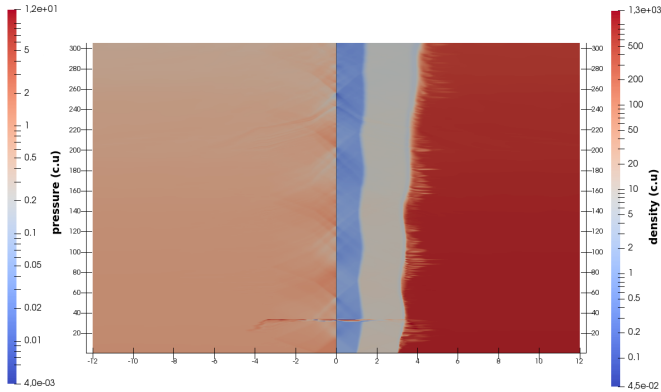


Figure 6: Snapshot: structured toroidal jet with an ejecta. Pressure map on the left, density map on the right. Units on x- and y-axis in 0.1 pc.

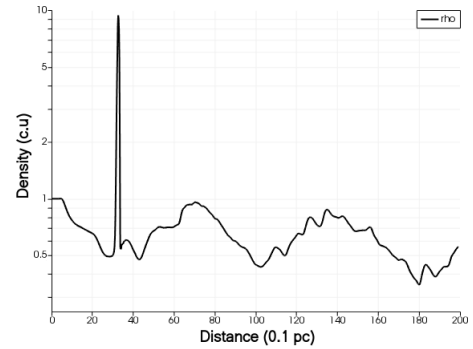


Figure 7: Profile of the density (log) in the inner jet along the propagation axis. Units on x-axis in 0.1 pc.

In the case of a toroidal large-scale structure of the magnetic field, the transverse density profile is very similar to the hydrodynamic case (Fig. 6, right). The impact of this magnetic configuration is felt along the azimuthal (φ angle) direction and not directly along the propagation axis. Again an ejecta was introduced (at a distance of ~ 3 pc, visible on the 1D profile on Fig. 7). The pressure map (Fig. 6, left) also resembles the hydrodynamic one, but in the toroidal configuration (field lines along φ , $B \sim 1$ mG), the moving shock induced by the ejecta is weaker compared to the poloidal case, and the transverse energy loss is decreased as well.

4. Emission maps and light curves

Following the study of the density and pressure profiles, we now want to determinate the impact of the magnetic configuration on the radiation emitted by the jet. Applying the post-processing step, we estimate the synchrotron emission maps in the radio band, assuming a population of electrons or pairs accelerated at the shocks (standing or moving). In the following applications, a viewing angle of 90° with respect to the jet axis is assumed.

4.1 The hydrodynamic case

Considering the presence of a turbulent component of the magnetic field in the hydrodynamic case, it is possible to estimate a map of the observed synchrotron flux at 1 GHz (Fig. 8). This map shows the presence of stationary shocks; the synchrotron flux depends on the strength of the magnetic field, which in this case depends on the thermal pressure. On Fig. 2 (left), one can see a succession of compression zones. In Fig. 8, we can also see a phenomenon of *edge-brightening* due to the gradient of density between the different components.

Interacting with the matter in the different components of the jet, the passage of the ejecta causes the appearance of a compression wave that accelerates the particles and causes the first observed flare ($t \sim 150$ years). From this moment, the ejecta begins to dissipate its energy and it can

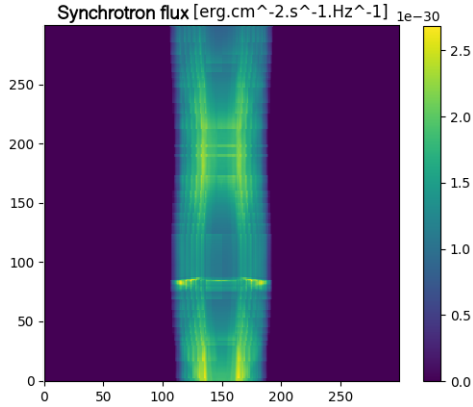


Figure 8: Synchrotron flux map with one ejecta.

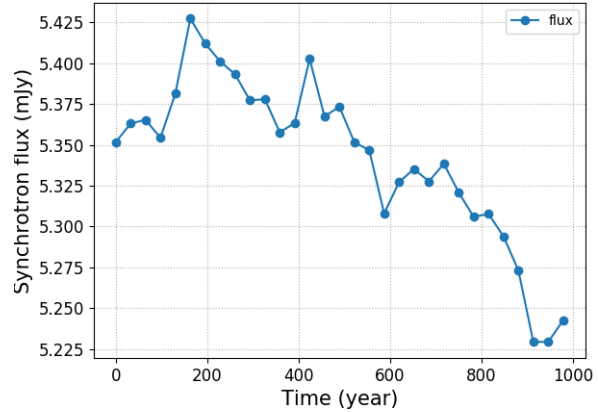


Figure 9: Light curve of the observed radio flux associated with the passage of an ejecta.

no longer maintain the compression wave, which causes the decrease of the observed synchrotron flux. The flux falls below the initial value (at $t \sim 500$ years) due to the self absorption of the ejecta travelling along the jet.

4.2 The poloidal case

On the synchrotron flux map of the poloidal case (Fig. 10), we can see the complex fine structure in stationary shocks caused by the magnetic pressure along the z -axis. On this map, one also sees a mobile compression zone associated with the ejecta. During its propagation, the transverse deformation is clearly visible and comes with a transverse dissipation of the energy. When the compression wave starts to interact with a denser medium (the OJ or the AM), it transfers its energy to the medium by accelerating the particles at the interface. In Fig. 11, a steep increase of the flux is visible (at $t \sim 300$ years), corresponding to the first interaction between the compression wave and a stationary shock. At this point, the ejecta seems to begin to dissipate its energy which explains the progressive decrease of the flux. There are other flares ($t \sim [500; 700; 900]$ years) due to the interaction of the compression wave with the other stationary shocks.

4.3 The toroidal case

Compared to the poloidal case, the map for the toroidal case in Fig. 12 shows a predominance of the synchrotron flux coming from the moving compression zone in front of the ejecta. As mentioned above, this magnetic configuration does not contribute along the z -axis, resulting in a synchrotron flux lower than in the poloidal case (globally a factor ~ 4 lower). The mobile compression zone leads to a local variation of the flux during the interaction with the stationary zones. Also, one can see that the transverse deformation of the ejecta is less pronounced. The light curve shows again a steep increase of the flux (at $t \sim 150$ years) with the first encounter between the compression zone and the first stationary shocks. In the toroidal case, the flux grows until the exit of the ejecta of the simulation box, while two others flares are visible (at $t \sim [450; 750]$ years).

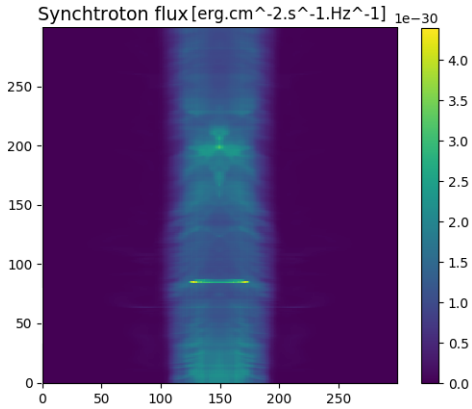


Figure 10: Synchrotron flux map with an ejecta.

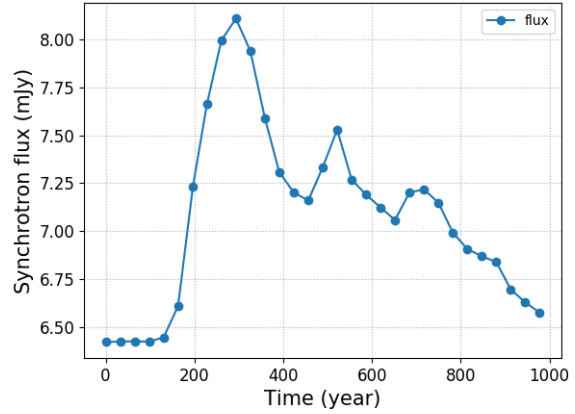


Figure 11: Observed light curve associated with the passage of an ejecta.

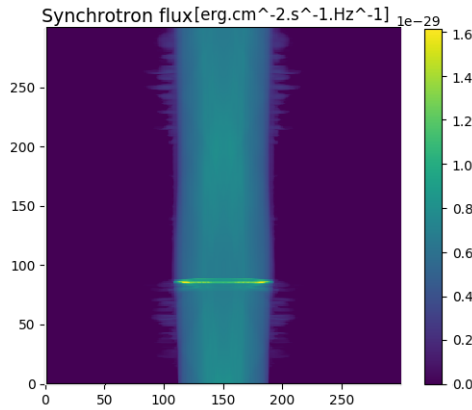


Figure 12: Synchrotron flux map with one ejecta.

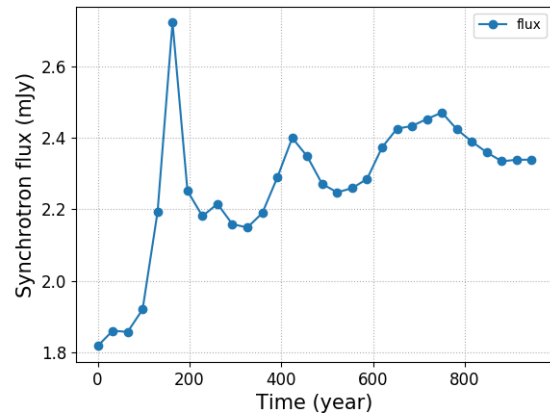


Figure 13: Light curve associated with the passage of one ejecta.

4.4 Comparison of the three cases

In summary, the presence of an external component of the jet will induce a diminution of the transverse deformation of the ejecta. Indeed, by limiting its expansion, the outer component of the jet will limit its energy dissipation.

The influence of a magnetic configuration is clearly visible, especially the presence of magnetic tension which will limit the transverse deformation of the ejecta. The poloidal case allows the appearance of a magnetic pressure along the z -axis which leads to a higher acceleration of the ejecta than in the toroidal case. This explains the difference in terms of synchrotron flux and in the time needed to observe a decrease in the light curve.

5. Application to a radio flare from M 87

Taking into account the above considerations, we apply our model to the compact jet of the well studied nearby radio galaxy M 87. A first objective is to reproduce a radio flare observed at the base of the jet [Acciaria et al. (2009)] in 2008. Previous studies on measuring the orientation of the magnetic field near the core of M 87 [Avachat et al. (2016)] [Walker et al. (2018)] are consistent with the utilisation of a toroidal two-component jet model and with recollimation shocks.

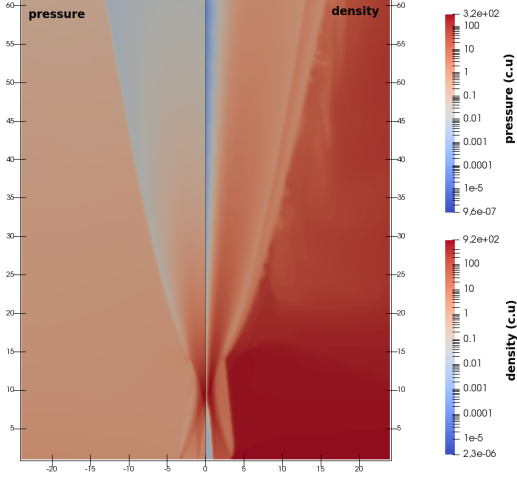


Figure 14: An open structured toroidal jet to simulate M 87.

We simulate the core region with a strong stationary compression zone at the base of the jet visible in Fig. 14. We take into account the observational constraints from [Walker et al. (2018)] and [Mertens et al. (2016)], in particular the opening angle of the jet ($\sim 50^\circ$) at its base. As the jet opens, a region of under-pressure will form, forcing the jet to re-collimate by creating a rarefaction zone in the inner jet.

To introduce the opening of the jet in our simulations, we impose an angle between the velocity along the z -axis and the r -axis in the outer jet. A more self-consistent solution would be to impose a negative gradient of density in the AM. The balance of pressures would then lead to an opening of the jet in a natural way, but this implies an in-depth parameter study to obtain an opening matching the observations and will be undertaken in a future phase of this work.

The flare is reproduced with an ejecta interacting with the strong stationary compression zone in the toroidal jet. Fig. 15 shows the simulated light curve compared to VLBA measurements. To obtain the light curve, the emitted flux was integrated over a region (1×1 pc) closely corresponding to the size of the point spread function of the radio beam. We obtain a result consistent with the observations in terms of measured flux and observed variability. The absence of observations of the flux decay makes it impossible to verify the simulated duration in this case.

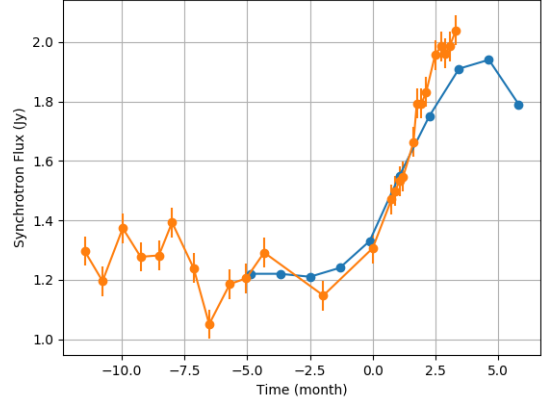


Figure 15: Observed radio light curve for M 87 with one ejecta in the observer frame. (orange: data from VLBA at 43 GHz; blue: our simulation)

6. Conclusions

In conclusion, we observe that the transverse structure of the jet greatly limits the lateral energy dissipation of the ejecta by reducing its interaction with the dense ambient medium. Furthermore, the magnetic configuration has been found to play an important role. Since it influences the structure of the stationary shocks, it will impact the lateral energy dissipation of the ejecta and the variability observed during the interactions. Furthermore, the presence of a magnetic pressure along the z -axis clearly increases the intensity of the observed synchrotron emission.

With the study of the different magnetic cases, a first application to a radio flare from M87 looks promising and will be extended to other wavebands. In fact, this particular flare was also seen at higher energies, in particular in the X-ray band (with Chandra) and in the VHE band (with the H.E.S.S., MAGIC and VERITAS Cherenkov telescopes). In a future extension of this work, an implementation of the radiative losses and a treatment of internal light travel time effects will be necessary to take into account the X-ray component of the synchrotron emission.

References

- [Acciaria et al. (2009)] Acciari, V.A. et al., 2009, *Science*, 325, 444
- [Asada et al. (2002)] Asada, K et al., 2002, *Publications of the Astronomical Society of Japan*, 54, L39-43
- [Avachat et al. (2016)] Avachat Sayali S. et al., 2016, *The Astrophysical Journal*, 832, 1
- [Giroletti et al. (2014)] Giroletti, M et al., 2014, *ApJ* 600, 1, 127–140
- [Gomez et al. (1995)] Gomez, J. Ma. et al., 1995, *The Astrophysical Journal*, 449, 19
- [Hervet et al.(2017)] Hervet, O., Meliani, Z., Zech, A., et al. 2017, 2017, *Astronomy & Astrophysics*, 606, A103
- [Katarzynski et al. (2001)] Katarzynski, K. et al., 2001, *Astronomy and Astrophysics*, 367, 809
- [Keppens et al. (2012)] Keppens, R. et al. , 2012, *Journal of Computational Physics*, 231, 718
- [Mertens et al. (2016)] Mertens, F. et al., 2016, *Astronomy & Astrophysics*, 595, 54
- [Motter et al. (2017)] Motter, J. C and Gabuzda, D. C., 2017, *Monthly Notices of the Royal Astronomical Society*, 467, 3, 2648-2663
- [Plotnikov et al. (2017)] Plotnikov, I. et al., 2017, *Monthly Notices of the Royal Astronomical Society*, 477, 5238
- [Siemiginowska et al. (2007)] Siemiginowska, A et al., 2007, *ApJ* 657, 1, 145–158
- [Toro et al. (1994)] Toro, E. F., Spruce, M. and Speares, W., 1994, *Shock Waves*, 4, 25–34
- [Walker et al. (2018)] Walker R. Craig, et al., 2018, *The Astrophysical Journal*, 485, 2